



Pyridine-N-rich Cu single-atom catalyst boosts nitrate electroreduction to ammonia

Yuanting Liu^a, Wenxi Qiu^a, Pengfei Wang^b, Ran Li^a, Kui Liu^a, Khalid M. Omer^c, Zhaoyu Jin^b, Panpan Li^{a,*}

^a College of Materials Science and Engineering, Sichuan University, Chengdu 610065, PR China

^b Institute of Fundamental and Frontier Sciences, University of Electronic Science and Technology of China, Chengdu 610054, PR China

^c Department of Chemistry, College of Science, University of Sulaimani, Sulaimani City, Kurdistan Region 46002, Iraq

ARTICLE INFO

Keywords:

Nitrate reduction reaction
Ammonia electrosynthesis
Single-atom catalysts
Pyridinic nitrogen
Polymer hydrogels

ABSTRACT

Nitrate-to-ammonia electroreduction (NO₃RR) offers a sustainable alternative to the energy-extensive Haber–Bosch process. Previous studies have reported nitrogen-coordinated copper single-atom catalysts with impressive activity and selectivity. However, regulating the nitrogen coordination structure at the atomic scale and its impact on the catalytic mechanism are not yet clear. This work demonstrates a pyridinic-N-rich copper single-atom catalyst (PR-CuNC) derived from semi-interpenetrating polypyrrole-polyethyleneimine hydrogels for the NO₃RR. By contrast to the catalyst with insufficient pyridinic nitrogen, PR-CuNC exhibits a maximum NH₃ Faraday efficiency of 94.61 % and a yield rate of 130.71 mg_{NH3} mg_{Cu}⁻¹ h⁻¹ (3.74 mg_{NH3} h⁻¹ cm⁻²). Theoretical evidence reveals that different N coordination types significantly affect the electronic structures of CuN₄ sites, resulting in the enhanced intrinsic activity. Our results show that the nitrogen structure is highly relevant to the performance of NO₃RR, underlining the importance of directly regulating the local coordination environment at the molecular level.

1. Introduction

Ammonia (NH₃), as an important raw material for fertilizers, pharmaceuticals, and chemical industries, is also considered a renewable energy carrier with the advantages of no carbon, high energy density (22.5 MJ kg⁻¹), and easy liquefaction [1–3]. Moreover, the conventional Haber–Bosch (H–B) process has dominated the synthetic ammonia industry and contributed to the rapid growth of the global population over the past century [4]. However, the H–B process requires high temperatures (400–500 °C) and high pressures (100–200 atm) to convert nitrogen (N₂) and hydrogen (H₂) into ammonia, resulting in annual energy consumption of about 5.5 EJ and greenhouse gas emissions of more than 450 million metric tons [5,6]. Due to the above defects of the H–B process, electrochemical N₂ reduction to NH₃ using H₂O instead of H₂ as a proton source has recently attracted significant attention owing to its mild reaction conditions [7,8]. Even so, the high dissociation energy of the N≡N bond (941 kJ mol⁻¹) and limited water solubility of N₂ leads to the aqueous-based N₂ reduction reaction suffering from inferior efficiency and yield [9–11]. In contrast, nitrate (NO₃) is more active than N₂

for NH₃ production due to the relatively lower dissociation energy of the N = O bond (204 kJ mol⁻¹), outstanding solubility, and favorable thermodynamic potential (0.69 V vs. RHE) [12]. Meanwhile, abundant NO₃ ions from agricultural and industrial discharge into the global hydrological environment may result in a series of hazards such as human diseases, eutrophication, ecosystem disruption, and even the imbalanced global nitrogen cycle [13–15]. Therefore, the reduction of NO₃ to NH₃ can promote the solution of environmental problems caused by NO₃ pollution and hopefully can be an alternative to the traditional ammonia synthesis process.

Electrochemical nitrate reduction to ammonia reaction involves a nine-proton coupled eight-electron transfer process, which obviously lowers the kinetic rate and leads to complex intermediates (e.g., NO₂) [12,16–18]. Moreover, the sluggish kinetic rate results in a considerable overpotential of NO₃RR, and thus the practical working potentials of NO₃RR are considerably overlaid with that of the hydrogen evolution reaction (HER) [19–22]. Therefore, the fierce competition between water/protons and reactants is inevitable during electrochemical NO₃RR. To this end, tremendous efforts have been devoted to tailoring

* Corresponding author.

E-mail address: panpanli@scu.edu.cn (P. Li).

<https://doi.org/10.1016/j.apcatb.2023.123228>

Received 9 June 2023; Received in revised form 16 August 2023; Accepted 24 August 2023

Available online 25 August 2023

0926-3373/© 2023 Elsevier B.V. All rights reserved.

structures of electrocatalysts from nano to atomic scale [23–26]. Compared with nanocatalysts, single-atom catalysts (SACs) demonstrate great potential in NO_3 -to- NH_3 conversion due to their maximum atomic utilization efficiency, unsaturated coordination environment, and tunable electronic structure [27,28]. Copper-based catalysts exhibit high catalytic activity for NO_3RR since Cu atoms with $3d^{10}$ orbital are more favorable for NO_3 adsorption [29,30]. Recently, N-doped carbon-based materials are used to anchor copper to achieve uniform dispersion of Cu atoms, serving as Cu-N-C single-atom catalysts [31–34]. Benefiting from the tunable structure of Cu-N-C SACs, regulating the local coordination environment of the Cu atom is an effective way to optimize the catalytic performance. Some previous reports have made substantial efforts to tune the metal-N-C construction from various dimensions including coordination number, first-shell and second-shell heteroatom doping, dual metal sites, and inter-site distance [24, 35–39]. Besides, direct regulation of the metal-coordinated N structure is a recently developed strategy, which has been studied in the oxygen reduction reaction (ORR) and the CO_2 reduction reaction (CO_2RR) [40, 41]. However, for the NO_3RR , the effect of the N structure on the selectivity of NH_3 and the competing HER is still unclear.

Herein, we report a pyridinic-N-rich coordinated copper single-atom catalyst (PR-CuNC) derived from three-dimensional (3D) semi-interpenetrating polypyrrole-polyethyleneimine (PPy-PEI) hydrogels with adsorbing Cu ions. Without introducing PEI, the structure of coordinated N was transformed to the relatively low pyridinic-N coordinated Cu (CuNC). PR-CuNC exhibits impressive Faraday efficiency of 94.61 % and a yield rate of $130.71 \text{ mg}_{\text{NH}_3} \text{ mg}_{\text{Cu}}^{-1} \text{ h}^{-1}$ for electrocatalytic NO_3RR , while the activity of CuNC is unsatisfactory. Theoretical evidence suggests that the electronic structure change originating from the Cu-N configuration is responsible for the enhanced catalytic performance. The favorable NO_3 adsorption and the lower energy barrier in the nitrate-to-ammonia reduction reaction of Cu-pyridinic- N_4 further support the experimental phenomenon from a thermodynamic perspective. The findings in this work highlight a new way to directly regulate the local nitrogen coordination environment for optimizing NO_3RR activity at the molecular level.

2. Experimental

2.1. Preparation of PEI-PPy hydrogels and PPy hydrogels

The semi-interpenetrating PEI-PPy hydrogels were prepared by the polymerization of pyrrole by introducing PEI in this strategy. Briefly, pyrrole monomers (0.3 M, 416 μL), PEI (0.101 g), and sodium dodecyl benzene sulfonate (SDBS, 0.1 M, 0.697 g) were dissolved in HCl aqueous solutions (1.0 M, 10 mL) and marked as solution A. Solution B was prepared by adding ammonium persulphate (APS, 0.3 M, 1.397 g) in HCl aqueous solutions (1.0 M, 10 mL). After cooling to 2 $^\circ\text{C}$, the above two solutions were rapidly mixed and left overnight at 2 $^\circ\text{C}$ to ensure complete polymerization. Finally, the as-prepared PEI-PPy hydrogels were alternately washed with deionized (DI) water and anhydrous ethanol several times to eliminate unreacted residual impurities and by-products. As a comparison, PPy hydrogels were also prepared in a similar process, in which PEI was absent in solution A.

2.2. Preparation of PR-CuNC and CuNC

The purified PEI-PPy hydrogels were added into copper chloride (0.2 M) aqueous solution with a continuous stirring for 12 h. Then, the PEI-PPy hydrogels with copper anions were washed several times with DI water and were treated by a freeze-drying process. Afterward, the obtained samples were ground into uniform powders and then calcined at 800 $^\circ\text{C}$ under flowing argon (Ar) for 2 h with a heating rate of 10 $^\circ\text{C} \text{ min}^{-1}$. After naturally cooling to room temperature, the powder products were further immersed in HCl solution (0.5 M) for 4 h at 80 $^\circ\text{C}$ to remove the unstable and inactivated copper clusters and particles. The

samples were subsequently washed with DI water until the pH value reached 7 and dried in a vacuum at 80 $^\circ\text{C}$. A second calcination was conducted under the same conditions and finally produced PR-CuNC. In contrast, CuNC was prepared via the same process for PR-CuNC unless PPy hydrogels were used. The catalyst (denoted as NC) derived from PPy-PEI hydrogel was prepared following the same process except for the absence of Cu ions adsorption.

2.3. Characterization

Scanning electron microscopy (SEM) was performed on a Helios G4 UC (Thermo Fisher Scientific, USA). High-angle annular dark-field scanning transmission electron microscopy (HAADF-STEM) images were obtained with a JEOL NEOARM probe-corrected transmission electron microscope with aberration correction (Japan). X-ray diffraction (XRD) patterns were recorded with a Rigaku Ultima IV X-ray diffraction system (Japan) using Cu K α radiation (40 kV / 40 mA, 10 $^\circ \text{ min}^{-1}$ from 5 $^\circ$ to 90 $^\circ$). X-ray photoelectron spectra (XPS) were acquired with Thermo Scientific K-Alpha (USA); all binding energies were referenced to the C 1s peak at 284.6 eV to correct the possible shift. X-ray absorption fine structure analysis (XAFS) based on synchrotron radiation was conducted at the BL14W1 beamline of the Shanghai Synchrotron Radiation Facility (China). The corresponding X-ray absorption near edge structure (XANES) and the extended X-ray absorption fine structure (EXAFS) were processed by using the IFEFFIT program package. The content of copper in the samples was determined by inductively coupled plasma atomic emission spectrometry (ICP-OES, Agilent 5110, USA). Ultraviolet-visible (UV-vis) absorption spectra were recorded using a Hitachi UV-2900 spectrophotometer (Japan). An online gas chromatography (GC 9790 II, FULI, China) equipped with a flame ionization detector (FID) and thermal conductivity detector (TCD) was used to monitor the gaseous products. All ^1H nuclear magnetic resonance (^1H NMR) spectra were collected on a Bruker Avance NEO 600 MHz (GER) with water suppression.

2.4. Electrochemical measurements

Electrochemical measurements were conducted on a DH7003 potentiostat (Donghua test, China) equipped with an H-type quartz electrochemical cell separated by Nafion 115 membrane. Before all tests, the Nafion 115 membranes with a size of 3.5 cm \times 3.5 cm were immersed in hydrogen peroxide solution (5 %) at 80 $^\circ\text{C}$ for 1 h and ultrapure water at 80 $^\circ\text{C}$ for another 1 h, respectively. The hydrophobic carbon paper was soaked in ethanol and DI water for 15 min with ultrasound treatment to remove surface impurities. The catalyst ink was prepared by adding 3 mg catalyst powder and 20 μL Nafion solution (5 wt%, Dupont, USA) into the mixture of DI water (360 μL) and isopropyl alcohol (120 μL) with ultrasonic treatment for 30 mins. Subsequently, homogeneous catalyst ink (20 μL) was drop-cast on hydrophobic carbon paper with an active area of 0.25 cm^2 and a mass loading of 0.48 $\text{mg} \text{ cm}^{-2}$. After the other side of the carbon paper without loading catalysts was sealed with an insulating hot-melt adhesive, the final working electrode was made. In addition, a saturated calomel electrode (SCE, 1 M KCl) and a graphite rod were used as the reference electrode and counter electrode, respectively. All potentials referenced to the reversible hydrogen electrodes (RHE) were obtained by the following calibration equation: $E(\text{RHE}) = E(\text{SCE}) + 0.059 \times \text{pH} + 0.253 \text{ V}$. Prior to electrochemical measurements, pure Ar-gas flow was injected into the 0.1 M KOH with or without 0.1 M NO_3 electrolytes for 30 mins to remove oxygen and nitrogen. All electrodes were activated by conducting cyclic voltammetry (CV) tests from +0.5 V to -0.9 V vs. RHE for 10 cycles at a scan rate of 100 $\text{mV} \text{ s}^{-1}$. Linear sweep voltammograms (LSVs) were acquired from +0.5 to -0.9 V vs. RHE at a scan rate of 10 $\text{mV} \text{ s}^{-1}$. The current-time (*I-t*) curves were recorded by the chronoamperometry methods, which were performed at different given potentials for 30 mins and the corresponding electrolytes were collected to calculate the yield

rate and Faraday efficiency of NH_3 . The electrochemical impedance spectroscopy (EIS) was performed at -0.2 V vs. RHE from 10^5 to 10^{-1} Hz.

3. Results and discussion

3.1. The preparation and characterization

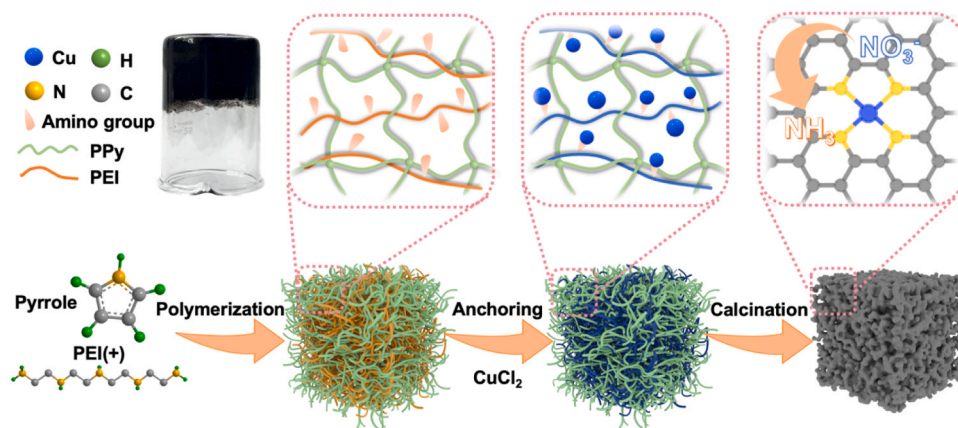
PR-CuNC was prepared through the pyrolysis of the PPy-PEI hydrogels with adsorbing Cu ions as illustrated in Scheme 1. Specifically, PEI was introduced in the polymerization of pyrrole to form PPy-PEI hydrogels, where PPy chains were uniformly interpenetrated with PEI chains. Benefiting from abundant primary and secondary amine groups of PEI, PPy-PEI hydrogels show the enhanced capability to anchor Cu ions compared with PPy only. However, the N site ($-\text{NH}-$) on the pyrrole five-membered ring is the only source of active N sites in PPy and is not conducive to anchoring metal atoms. Cross-linking pyrrole with PEI effectively improved scarce nitrogen active sites and provided diverse coordination environments. Besides, PPy-PEI hydrogels possess a unique 3D semi-interconnected nanostructure with abundant N sites and large surface area, facilitating Cu ions adsorption and preventing aggregated Cu particles during subsequent carbonization. Finally, copper-adsorbed PPy-PEI hydrogels were calcined to produce a PR-CuNC in which the highly dispersed Cu atoms were anchored on the hydrogel-derived carbon substrate.

As shown in Fig. 1a, the PR-CuNC possesses a porous granular structure composed of interconnected nanoparticles, which is similar to that of CuNC and NC (Fig. S1). In Fig. S2, the XRD pattern of PR-CuNC displays a broad peak at 25.6° corresponding to the (002) plane of graphitic carbon, while no diffraction peaks from Cu-based crystal phases are observed. Thus, there are no aggregated Cu-based compounds existing in PR-CuNC, and Cu species are mainly amorphous. Additionally, CuNC shows similar XRD features as PR-CuNC (Fig. S2). Besides, the Brunauer–Emmett–Teller (BET) surface area of PR-CuNC ($240.58 \text{ m}^2 \text{ g}^{-1}$) is similar to that of CuNC ($277.72 \text{ m}^2 \text{ g}^{-1}$, Table S1). Based on the above characterization results, it can be concluded that the introduction of PEI has little effect on the morphology and crystal plane structures, eliminating the influence of carbon substrate on material properties. High-angle annular dark field scanning transmission electron microscopy (HAADF-STEM) with aberration correction was carried out to identify the distribution of atoms. As depicted in Fig. 1b, the HAADF-STEM image of PR-CuNC exhibits light spots dispersed on the edge and surface of the carbon substrate. Since the atom mass of the Cu element is much larger than that of other elements (C, N, O, see the XPS results in Fig. S3) in the catalyst, it can be determined that the light spots represent isolated Cu single atoms. Energy dispersive X-ray spectroscopy (EDS) mapping analysis further confirms the homogeneous dispersion of Cu, N,

and C elements in PR-CuNC, suggesting that Cu atoms were uniformly distributed on the nitrogen-doped carbon substrate.

X-ray photoelectron spectroscopy (XPS) measurement was conducted to determine the elemental composition and valence state of catalysts. According to XPS survey spectra (Fig. S3), the elemental composition and atomic ratios of PR-CuNC, CuNC, and NC were confirmed and summarized in Table S2. The atomic ratio of the N element in PR-CuNC is 8.21 % higher than that in CuNC (6.48 %), which can be attributed to the presence of PEI with rich amine groups. As shown in Fig. 1d, the high-resolution N 1s XPS spectra for PR-CuNC and CuNC can be deconvoluted into four peaks ascribed to pyridinic-N (398.2 eV), pyrrolic-N (399.3 eV), graphite-N (400.8 eV) and oxidized-N (401.7 eV) [41–43]. The N 1s XPS spectrum of NC is depicted in Fig. S4. The percentages of four nitrogen species are summarized in Table S3 and S4, where PR-CuNC and CuNC both show similar contents of pyridinic-N and oxidized-N. However, the absolute content of pyridinic-N on PR-CuNC is 3.20 % exceeding that on CuNC (1.99 %), while PR-CuNC shows a lower absolute content of pyrrolic-N (0.76 %) than CuNC (1.16 %). It suggests that the introduction of PEI successfully boosts the pyridinic-N ratio, forming more Cu-pyridinic-N coordination configuration in PR-CuNC. For the Cu 2p XPS spectrum, PR-CuNC (Fig. S5a) exhibits double characteristic peaks of Cu $2p_{3/2}$ and Cu $2p_{1/2}$, which both are deconvoluted into two peaks corresponding to Cu^{2+} species (934.55 and 954.40 eV) and $\text{Cu}^{1+}/\text{Cu}^0$ species (932.40 and 952.14 eV) [44]. The Cu 2p XPS spectrum for CuNC in Fig. S5b shows similar peaks assigned to Cu^{2+} and $\text{Cu}^{1+}/\text{Cu}^0$, respectively [45]. The accurate Cu content is further determined by inductive coupled plasma-optical emission spectroscopy (ICP-OES) in Table S5, where PR-CuNC (6.01 wt%) is higher than CuNC (3.69 wt%) probably owing to the strong binding ability of PEI.

Due to the accuracy of XPS being insufficient for analyzing Cu species with low content, the chemical and atomic structure of Cu sites in PR-CuNC were further investigated by synchrotron X-ray absorption spectroscopy (XAS). Fig. 1e illustrates Cu K-edge X-ray absorption near edge structure (XANES) spectra of PR-CuNC and several reference samples. In comparison to Cu_2O and Cu foil, the adsorption edge for PR-CuNC is located at a higher energy close to CuO, indicating Cu atoms are in an oxidized state. The first derivative of PR-CuNC is between that of Cu_2O and CuO (in the inset of Fig. 1e), which confirms that the valence state of Cu for PR-CuNC is between +1 and +2, consistent with the observation from the Cu 2p XPS of PR-CuNC [21,28]. The Fourier-transformed X-ray absorption fine structure (FT-EXAFS) spectra were obtained to verify the accurate structure of Cu atoms in PR-CuNC displayed in Fig. 1f. Cu foil reveals a main peak at around 2.24 \AA corresponding to the Cu-Cu bond. In contrast, PR-CuNC only shows a single peak centered at 1.45 \AA assigned to the Cu-N bond, differing from the Cu-O bond in CuO and Cu_2O [46]. It confirms that Cu atoms in PR-CuNC are separated from



Scheme 1. The synthetic route of the PR-CuNC.

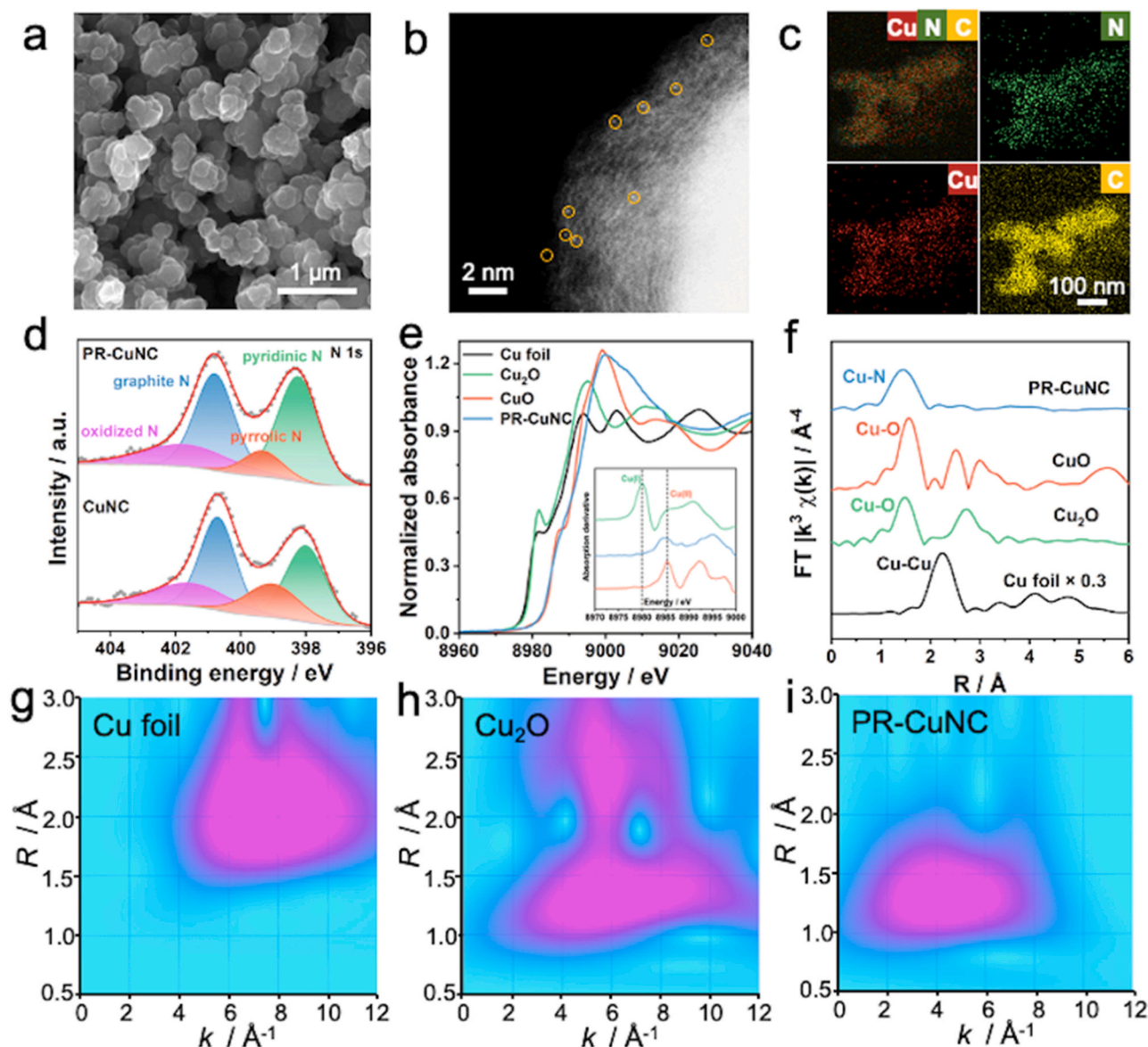


Fig. 1. Morphology, structure, and compositions. (a) SEM, (b) HAADF-STEM, and (c) EDS element mapping images of PR-CuNC. (d) N 1s XPS spectra of PR-CuNC and CuNC. (e) Normalized XANES of Cu K-edge, derivatives of XANES (inset), and (f) EXAFS of Cu foil, Cu₂O, and CuO and PR-CuNC. WT plots of Cu K-edge EXAFS spectra for (g) Cu foil, (h) Cu₂O, and (i) PR-CuNC.

each other and coordinated with first-shell N atoms, which is in agreement with the result of the HAADF-STEM. Besides, the best fitting results of EXAFS k and R -space provide detailed structural parameters in Fig. S6 and Table S6. According to the coordination number of 4.54, the Cu atom was bonded by four N atoms with Cu-N bonds, implying the Cu-N₄ configurations in PR-CuNC. On the contrary, the model of Cu coordinated with pyrrolic nitrogen shows worse fitting results in Fig. S7, indicating that Cu atoms in PR-CuNC were more coordinated with pyridinic-N, which is consistent with XPS results. Moreover, wavelet transfer (WT) plots in Fig. 1g-i were applied to better visualize the Cu-K edge EXAFS oscillations. Cu foil depicts an intensity maximum at around 8 \AA^{-1} belonging to the Cu-Cu bond. In contrast, the only intensity maximum of PR-CuNC is observed at 4 \AA^{-1} assigning to the Cu-N bond, which slightly differs in the Cu-O bond (about 6 \AA^{-1}) in Cu₂O [47].

3.2. Electrochemical performance for the NO₃RR

The electrochemical measurements for NO₃ reduction reaction were conducted in H-cell using Ar-saturated 0.1 M KOH with and without

0.1 M KNO₃ as electrolytes. Fig. 2a shows the LSV curves for PR-CuNC, CuNC, and NC. After adding NO₃, the current densities for all samples improve dramatically, demonstrating the occurrences of the NO₃RR. Compared with CuNC and NC, PR-CuNC reaches a relatively high current density of 90 mA cm^{-2} at -0.9 V vs. RHE and a low onset potential of $+0.1 \text{ V}$ vs. RHE, indicating superior activity for nitrate reduction. Moreover, a small reduction peak at 0.0 V vs. RHE and another wide reduction peak at around -0.5 V vs. RHE belong to the NO₃-to-NO₂ reduction and NO₂-to-NH₃ process [21,48]. Additionally, EIS tests were conducted on PR-CuNC and CuNC to measure the charge-transfer resistances during the electrochemical NO₃RR process. As shown in Fig. S8, the Nyquist plots displays PR-CuNC with a smaller semicircle diameter and charge transfer resistance (23.21 \Omega) than that of CuNC (42.29 \Omega) at -0.2 V vs. RHE, suggesting a faster kinetics rate for the NO₃RR.

To further evaluate the NO₃RR performance, current density-time (I - t) curves of all samples from -0.1 to -0.6 V vs. RHE were recorded (Fig. S9). Then, the amount of produced NH₃ in electrolytes after I - t tests were determined by the indophenol blue spectrophotometric method for

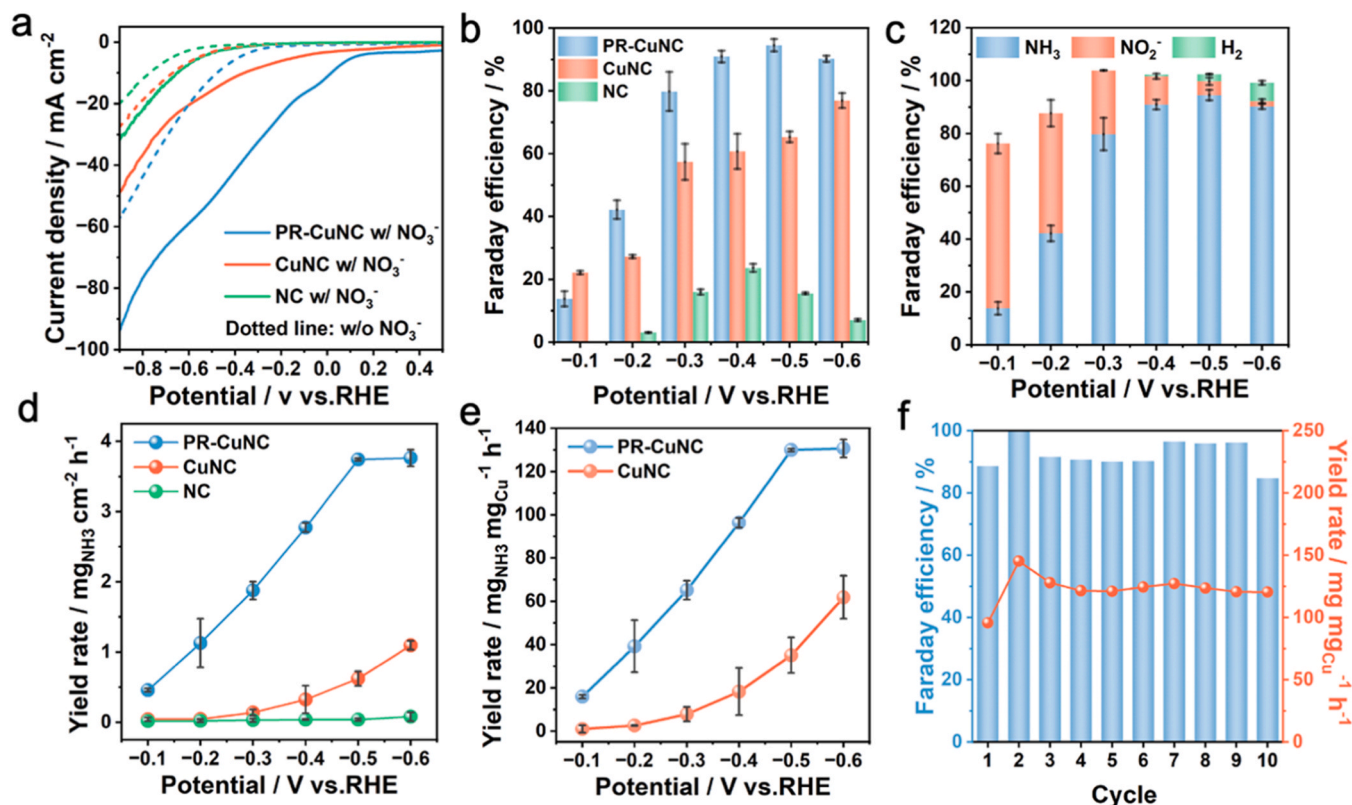


Fig. 2. Electrocatalytic performance of different catalysts for NO₃RR. (a) LSVs of PR-CuNC, CuNC, and NC with and without NO₃⁻. (b) FE of NH₃ for PR-CuNC, CuNC and NC. (c) FE of NH₃, NO₂⁻ and H₂ for PR-CuNC. (d) Y_{RA} for PR-CuNC, CuNC and NC. (e) Y_{RCu} for PR-CuNC and CuNC. (f) The catalytic durability of PR-CuNC.

calculating Faraday efficiency (FE, Fig. S10). As shown in Fig. 2b, PR-CuNC outperforms all catalysts at almost all potentials, reaching a maximum FE of 94.61 %. In contrast, CuNC displays inferior activity with a maximum FE of 76.99 %, implying that rich Cu-pyridinic-N coordination configuration in PR-CuNC significantly enhances the NO₃RR activity. Furthermore, Cu-NC catalysts with higher or lower pyridinic-N content (denoted as HP-Cu-NC and LP-Cu-NC) were obtained by introducing PEI with different concentrations (Fig. S11 and Table S7). Electrochemical nitrate reduction experiments in a 0.1 M KOH and 0.1 M KNO₃ electrolyte showed that as the pyridinic-N content increased, the FE also increased, supporting our previous interpretation (Fig. S12). While NC has almost no catalytic capacity for NO₃RR, the NH₃ production is nearly negligible at less than 30 %, suggesting that Cu sites are the dominant active sites remarkably contributing to the nitrate-to-ammonia conversion. When the applied potential for PR-CuNC is below -0.5 V vs. RHE, the Faraday efficiency of NH₃ decreases even though the total current density continues to increase, indicating that other side reactions weaken the ammonia production rate. The complex NO₃RR process is associated with a variety of nitrogenous byproducts such as NO₂, N₂, N₂H₄, and NO_x, accompanied by fierce competition with the HER. It is therefore necessary to detect the FE of major products (NO₂ and H₂) for further evaluation of selectivity. As depicted in Fig. 2c, NO₂ is the primary product at low overpotential for PR-CuNC. With applied a more negative potential, the FE of NO₂ gradually decreased, which can be contributed to the NO₂-to-NH₃ reduction wide peak at near -0.5 V vs. RHE (Fig. 2a). Moreover, the competitive HER affects NH₃ selectivity from -0.4 V, and the maximum Faraday efficiency reaches 6.92 % at -0.6 V on PR-CuNC. The same product analysis of CuNC and NC was conducted and shown in Fig. S13. As with PR-CuNC, the major byproduct of CuNC and NC changes from NO₂ and H₂ as the overpotential rises, while the FE values of H₂ in two samples are much higher, reaching 22.38 % and 17.65 % at -0.6 V vs. RHE, respectively. Consequently, pyridinic-N-rich Cu sites in PR-CuNC can effectively

suppress the HER and NO₂ formation during high overpotential, which greatly facilitates the NH₃ generation from NO₃. Meanwhile, the yield rates based on the geometric area of electrodes (Y_{RA}) (see details in supporting information) of different catalysts were detected at varying potentials (Fig. 2d). PR-CuNC demonstrates a much higher Y_{RA} of 3.74 mg_{NH₃} h⁻¹ cm⁻² at -0.5 V vs. RHE than that of CuNC (1.10 mg_{NH₃} h⁻¹ cm⁻²) and NC (0.08 mg_{NH₃} h⁻¹ cm⁻²). To avoid the contribution from the Cu content, the YR was normalized by the mass of Cu labeled as Y_{RCu} in PR-CuNC and CuNC (see details in supporting information). As shown in Fig. 2e, PR-CuNC achieves 130.71 mg_{NH₃} mg_{Cu}⁻¹ h⁻¹ at -0.5 V vs. RHE, which outperforms CuNC with the Y_{RCu} of 71.87 mg_{NH₃} mg_{Cu}⁻¹ h⁻¹. Combining the XPS results, the enhanced FE and YR of PR-CuNC over CuNC could be ascribed to the increased pyridinic-N structure. Notably, the NO₃RR performance of PR-CuNC at a relatively low overpotential is superior to most reported single-atom catalysts which be summarized in Table S8.

The catalyst stability during the electrochemical process of NO₃RR is a crucial factor in measuring the quality and applicability of catalysts. Therefore, ten consecutive electrolysis experiments were carried out at -0.5 V vs. RHE using the same electrode and further calculated the FE and Y_{RCu} to investigate the durability of PR-CuNC. After 10 cycles, FE is consistently higher than 85 % and YR remains stable above 120 mg_{NH₃} mg_{Cu}⁻¹ h⁻¹ (Fig. 2f), demonstrating convincingly the excellent electrochemical recyclability of PR-CuNC. The initial improvement of catalytic performance might be attributed to the catalyst on the electrode surface being fully activated after electrolysis and then gradually reaching a steady state (Fig. S14). In addition to electrochemical stability, the structural stability of the PR-CuNC was also evaluated. As shown in Fig. S15, SEM images showed that the catalyst after tests still exhibited a porous granular structure, which was similar to PR-CuNC before tests. Besides, no aggregation of Cu atoms was observed in TEM images (Fig. S16 and S17), suggesting the morphology of the catalyst barely changed. According to XPS survey spectra (Fig. S18), the area of the

double characteristic peaks assigned to $\text{Cu}^{1+}/\text{Cu}^0$ increased after NO_3RR tests, while that of Cu^{2+} became smaller, implying the reduction of Cu^{2+} to $\text{Cu}^{1+}/\text{Cu}^0$ during the NO_3RR .

Additionally, the ^{15}N isotope labeling proton nuclear magnetic resource (^1H NMR) was performed to verify the precision of the NH_3 measurements and eliminate the possible ammonia contamination from the environment. Electrochemical tests were conducted using $^{14}\text{NO}_3^-$ and $^{15}\text{NO}_3^-$ as nitrate sources, respectively. Fig. S19a exhibits different ^1H NMR spectra of ammonia synthesized from different nitrate sources. $^{14}\text{NH}_4^+$ owns triple peaks with a spacing of 52 Hz, while $^{15}\text{NH}_4^+$ shows characteristic double peaks with a spacing of 72 Hz. Meanwhile, maleic acid was used as an internal standard for quantifying the generated ammonia. As shown in Fig. S19b, the yield of produced $^{15}\text{NH}_4^+$ (17.04 μmol) is very close to that of $^{14}\text{NH}_4^+$ (16.92 μmol), implying that the NH_3 determined in this work only derived from the electrocatalytic nitrate process. Moreover, the amount of ammonia quantified by ^1H NMR (16.92 μmol) is comparable to that detected by the UV-Vis method (16.96 μmol), confirming the reliability of the results from indophenol blue spectrophotometry.

3.3. Theoretical understanding of the catalytic mechanism

To further understand the mechanistic insights of the superior nitrate selectivity exhibited by the pyridinic-N-rich Cu SACs, density functional theory (DFT) calculations were conducted to investigate the structure-activity relationship. XANES and EXAFS results indicate the center Cu atom is isolated and coordinated to the surrounding N. Herein, we constructed two Cu-N_4 catalyst models, in which Cu single atoms are coordinated with four pyridinic-N (Cu-pyridinic- N_4) and four pyrrolic-N (Cu-pyrrolic- N_4), respectively. The charge density differences of the above two Cu-N_4 models are illustrated in Fig. 3a–b, which depict obviously different charge distributions. Compared to Cu-pyrrolic- N_4 , Cu-pyridinic- N_4 exhibits a change in electron depletion around the Cu atom and a stronger electron accumulation around C atoms bonded to N.

Moreover, the partial densities of states (PDOS) of Cu-pyridinic- N_4 and Cu-pyrrolic- N_4 were presented in Fig. 3c. Cu d orbital of Cu-pyridinic- N_4 has obvious energy level splitting near the Fermi level and the negative shift of the active center compared to that of Cu-pyrrolic- N_4 . Due to apparent hybridization between Cu d and N p orbitals as well as the higher overlap regions of electron density at the bonding orbitals, the Cu-pyridinic- N_4 type is more favorable to electron transfer and is more active for adsorbed NO_3^- . The different distributions of state density demonstrate that the electronic structure of Cu- N_4 is regulated by the types of coordination N.

The catalytic details for NO_3RR are obtained by the Gibbs free energy diagram. The element steps including nine elementary steps and eight intermediates as considered based on the previously reported mechanism [1,12,49]. Moreover, the geometry structures of all intermediates generated on the Cu- N_4 were optimized before thermodynamic calculations (as the bottom of Fig. 3d). The first step in adsorbing NO_3^- to give $^*\text{NO}_3$ is considered crucial, as it matters whether the reaction can begin spontaneously. As shown in Fig. 3d, the adsorption energy of NO_3^- (ΔG_{NO_3}) substantially declines to -2.06 eV on Cu-pyridinic- N_4 , while the ΔG_{NO_3} declines to -2.53 eV on Cu-pyrrolic- N_4 , indicating that Cu-pyridinic- N_4 was more advantageous for NO_3^- adsorption. Then, as two N-O bonds on $^*\text{NO}_3$ break in sequence to form $^*\text{NO}_2$ and $^*\text{NO}$, the energy gradually decreases. However, a large energy barrier needs to be overcome in the subsequent hydrogenation process, referring to the step from $^*\text{NO}$ to $^*\text{NHO}$. Cu-pyridinic- N_4 shows a lower $\Delta G_{^*\text{NHO}}$ of $+0.07$ eV than Cu-pyrrolic- N_4 ($+0.51$ eV), implying that Cu-pyridinic- N_4 is more active for the protonation of $^*\text{NO}$. Subsequently, two successive protonation steps of $^*\text{NHO}$ and cleavage of N-O bonds generate $^*\text{NH}_2$, followed by a hydrogenation process to obtain adsorbed $^*\text{NH}_3$. Finally, $^*\text{NH}_3$ undergoes a desorption step from the catalyst surface to produce the free NH_3 , completing the whole nitrate reduction reaction to ammonia. Overall, the NO_3RR steps are exothermic except for the $^*\text{NHO}$ formation, which is considered a rate-limiting step. The larger ΔG_{NO_3} and the lower energy barrier of the rate-limiting step indicate that the

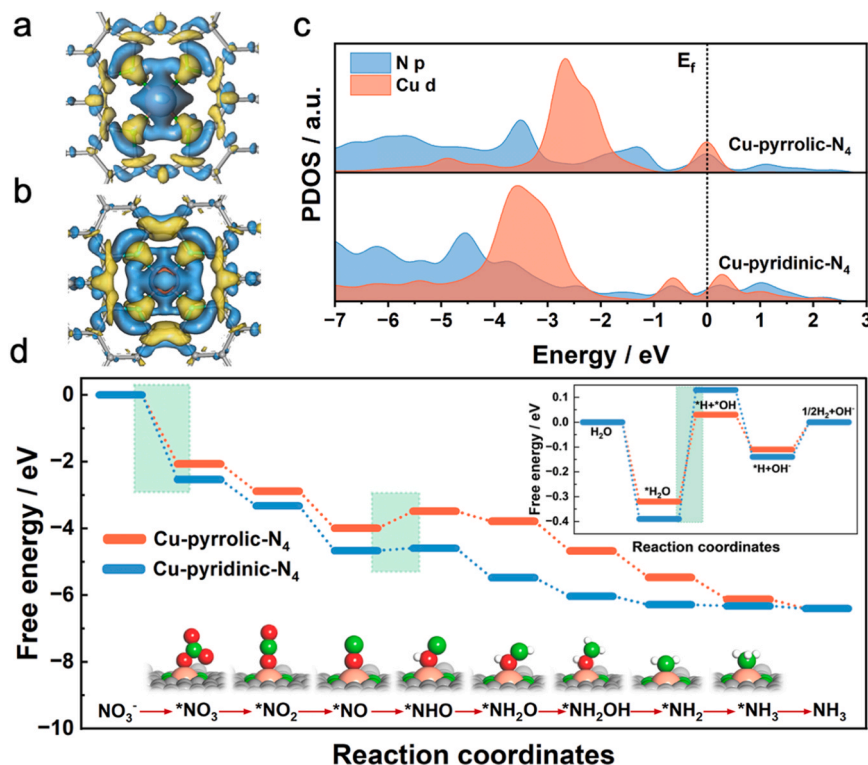


Fig. 3. DFT calculations. The charge density difference of (a) Cu-pyrrolic- N_4 and (b) Cu-pyridinic- N_4 . (blue: accumulated electron density; yellow: depleted electron density; the isosurface value: $0.002 \text{ e } \text{\AA}^{-3}$). (c) PDOS of Cu d and N p of the Cu-pyrrolic- N_4 and Cu-pyridinic- N_4 sites. (d) The Gibbs free energy diagram of nitrate reduction to ammonia and water dissociation (the top right) on Cu-pyrrolic- N_4 and Cu-pyridinic- N_4 sites.

Cu-pyridinic-N₄ structure is more favorable for ammonia synthesis from NO₃⁻. The Gibbs free energy diagrams of HER on Cu-pyridinic-N₄ and Cu-pyrrolic-N₄ were analyzed in the top right of Fig. 3d. The higher ΔG_{H_2O} of Cu-pyridinic-N₄ (0.39 eV) than that of Cu-pyrrolic-N₄ (0.32 eV), suggesting a more favorable capability for capturing H₂O molecules effectively. Furthermore, the decomposition of *H₂O is considered a rate-determining step, where the larger energy barrier ($\Delta G=0.52$ eV) observed on the Cu-pyridinic-N₄ demonstrates the suppressed HER compared with the Cu-pyrrolic-N₄ surface ($\Delta G=0.35$ eV).

4. Conclusion

In summary, a hydrogel-derived pyridinic-N-rich Cu single-atom catalyst was synthesized in this work by successfully regulating the structure of coordination N atoms. The absolute content of pyridinic-N increases from 1.99 % to 3.20 % by forming semi-interpenetrating PPy-PEI hydrogels with abundant N sites. Efficient NO₃⁻-to-NH₃ reduction was achieved on PR-CuNC at low overpotentials, reaching a maximal Faraday efficiency of 94.61 % and a yield rate of 130.71 mg_{NH3} mg_{Cu}⁻¹ h⁻¹. According to NO₃⁻ reduction experiments and DFT calculations, we disclose that the high NO₃RR activity and selectivity for NH₃ of PR-CuNC originated from the single-atom Cu sites coordinated with four pyridinic-N atoms. Importantly, the different charge density differences and PDOS of Cu-pyrrolic-N₄ and Cu-pyridinic-N₄ demonstrate the change in electron structure between Cu and N atoms. Compared to Cu-pyrrolic-N₄, the Cu-pyridinic-N₄ has a more advantageous NO₃⁻ adsorption ability and lower energy barrier for protonating *NO to *NHO during the NO₃RR reaction steps. This study highlights a strategy to directly regulate the local nitrogen microenvironment of single-atom catalysts at the molecular scale. This work also provides a deeper understanding of the essential relationship between the coordination environment of the atomic site and catalytic behavior for various catalytic reactions.

CRediT authorship contribution statement

Yuanting Liu: Validation, Formal analysis, Investigation, Writing – original draft. **Wenxi Qiu:** Validation, Formal analysis. **Pengfei Wang:** Resources. **Ran Li:** Validation. **Kui Liu:** Resources. **Khalid M. Omer:** Resources. **Zhaoyu Jin:** Formal analysis, Writing – review & editing. **Panpan Li:** Conceptualization, Supervision, Methodology, Project administration, Funding acquisition, Writing – review & editing.

Declaration of Competing Interest

The authors declare the following financial interests/personal relationships which may be considered as potential competing interests: Panpan Li reports financial support was provided by National Natural Science Foundation of China. Panpan Li reports financial support was provided by Sichuan Province Science and Technology Support Program.

Data Availability

Data will be made available on request.

Acknowledgments

We gratefully acknowledge financial support from the National Nature Science Foundation of China (No. 52202372), Sichuan Science and Technology Program (Nos. 2023NSFSC0436 and 2023NSFSC0089), and Fundamental Research Funds for the Central Universities (Nos. YJ2021151 and 20826041G4185). We also acknowledge Hui Wang from the Analytical & Testing Center of Sichuan University for SEM imaging. We thank Sheng Liu from Shiyanjia Lab (www.shiyanjia.com) for the XPS analysis.

Appendix A. Supporting information

Supplementary data associated with this article can be found in the online version at supporting information.

Appendix A. Supporting information

Supplementary data associated with this article can be found in the online version at [doi:10.1016/j.apcatb.2023.123228](https://doi.org/10.1016/j.apcatb.2023.123228).

References

- [1] P.H. van Langevelde, I. Katsounaros, M.T.M. Koper, Electrocatalytic nitrate reduction for sustainable ammonia production, *Joule* 5 (2021) 290–294, <https://doi.org/10.1016/j.joule.2020.12.025>.
- [2] A. Valera-Medina, H. Xiao, M. Owen-Jones, W.I.F. David, P.J. Bowen, Ammonia for power, *Prog. Energy Combust. Sci.* 69 (2018) 63–102, <https://doi.org/10.1016/j.pecs.2018.07.001>.
- [3] C.H. Christensen, T. Johannessen, R.Z. Sørensen, J.K. Nørskov, Towards an ammonia-mediated hydrogen economy? *Catal. Today* 111 (2006) 140–144, <https://doi.org/10.1016/j.cattod.2005.10.011>.
- [4] G.V. Duine, How a century of ammonia synthesis changed the world, *Nat. Geosci.* 1 (2008) 4.
- [5] L. Wang, M. Xia, H. Wang, K. Huang, C. Qian, C.T. Maravelias, G.A. Ozin, Greening ammonia toward the solar ammonia refinery, *Joule* 2 (2018) 1055–1074, <https://doi.org/10.1016/j.joule.2018.04.017>.
- [6] J. Lim, C.A. Fernández, S.W. Lee, M.C. Hatzell, Ammonia and nitric acid demands for fertilizer use in 2050, *ACS Energy Lett.* 6 (2021) 3676–3685, <https://doi.org/10.1021/acsenergylett.1c01614>.
- [7] G. Soloveichik, Electrochemical synthesis of ammonia as a potential alternative to the Haber–Bosch process, *Nat. Catal.* 2 (2019) 377–380, <https://doi.org/10.1038/s41929-019-0280-0>.
- [8] C. Guo, J. Ran, A. Vasileff, S.-Z. Qiao, Rational design of electrocatalysts and photo (electro)catalysts for nitrogen reduction to ammonia (NH₃) under ambient conditions, *Energy Environ. Sci.* 11 (2018) 45–56, <https://doi.org/10.1039/C7EE02220D>.
- [9] B.H.R. Suryanto, H.-L. Du, D. Wang, J. Chen, A.N. Simonov, D.R. MacFarlane, Challenges and prospects in the catalysis of electroreduction of nitrogen to ammonia, *Nat. Catal.* 2 (2019) 290–296, <https://doi.org/10.1038/s41929-019-0252-4>.
- [10] D.R. MacFarlane, P.V. Cherepanov, J. Choi, B.H.R. Suryanto, R.Y. Hodgetts, J. M. Bakker, F.M. Ferrero Vallana, A.N. Simonov, A roadmap to the ammonia economy, *Joule* 4 (2020) 1186–1205, <https://doi.org/10.1016/j.joule.2020.04.004>.
- [11] V. Kordali, G. Kyriacou, Ch Lambrou, Electrochemical synthesis of ammonia at atmospheric pressure and low temperature in a solid polymer electrolyte cell, *Chem. Commun.* (2000) 1673–1674, <https://doi.org/10.1039/b004885m>.
- [12] P. Li, Z. Jin, Z. Fang, G. Yu, A single-site iron catalyst with preoccupied active centers that achieves selective ammonia electrosynthesis from nitrate, *Energy Environ. Sci.* 14 (2021) 3522–3531, <https://doi.org/10.1039/D1EE00545F>.
- [13] N. Gruber, J.N. Galloway, An Earth-system perspective of the global nitrogen cycle, *Nature* 451 (2008) 293–296, <https://doi.org/10.1038/nature06592>.
- [14] X. Zou, J. Xie, C. Wang, G. Jiang, K. Tang, C. Chen, Electrochemical nitrate reduction to produce ammonia integrated into wastewater treatment: investigations and challenges, *Chin. Chem. Lett.* 34 (2023), 107908, <https://doi.org/10.1016/j.cclet.2022.107908>.
- [15] Y. Liu, K. Liu, P. Wang, Z. Jin, P. Li, Electrocatalytic upcycling of nitrogenous wastes into green ammonia: advances and perspectives on materials innovation, *Carbon Neutrality* 2 (2023) 14, <https://doi.org/10.1007/s43979-023-00055-7>.
- [16] S. Garcia-Segura, M. Lanzarini-Lopes, K. Hristovski, P. Westerhoff, Electrocatalytic reduction of nitrate: fundamentals to full-scale water treatment applications, *Appl. Catal. B Environ.* 236 (2018) 546–568, <https://doi.org/10.1016/j.apcatb.2018.05.041>.
- [17] Z. Jin, High-spatiotemporal-resolution electrochemical measurements of electrocatalytic reactivity, *Anal. Chem.* 95 (2023) 6477–6489, <https://doi.org/10.1021/acs.analchem.2c05755>.
- [18] Z. Jin, P. Li, Z. Fang, G. Yu, Emerging electrochemical techniques for probing site behavior in single-atom electrocatalysts, *Acc. Chem. Res.* 55 (2022) 759–769, <https://doi.org/10.1021/acs.accounts.1c00785>.
- [19] A.R. Singh, B.A. Rohr, J.A. Schwalbe, M. Cargnello, K. Chan, T.F. Jaramillo, I. Chorkendorff, J.K. Nørskov, Electrochemical ammonia synthesis—the selectivity challenge, *ACS Catal.* 7 (2017) 706–709, <https://doi.org/10.1021/acscatal.6b03035>.
- [20] P. Wang, Z. Jin, P. Li, G. Yu, Design principles of hydrogen-evolution-suppressing single-atom catalysts for aqueous electrosynthesis, *Chem. Catal.* 2 (2022) 1277–1287, <https://doi.org/10.1016/j.cheecat.2022.04.020>.
- [21] P. Li, R. Li, Y. Liu, M. Xie, Z. Jin, G. Yu, Pulsed nitrate-to-ammonia electroreduction facilitated by tandem catalysis of nitrite intermediates, *J. Am. Chem. Soc.* 145 (2023) 6471–6479, <https://doi.org/10.1021/jacs.3c00334>.
- [22] W. Qiu, M. Xie, P. Wang, T. Gao, R. Li, D. Xiao, Z. Jin, P. Li, Size-defined Ru nanoclusters supported by TiO₂ nanotubes enable low-concentration nitrate

- electroreduction to ammonia with suppressed hydrogen evolution, *Small* (2023) 2300437, <https://doi.org/10.1002/smll.202300437>.
- [23] Y. Zhang, S. Li, W. Zheng, X. Wang, Computational design of catalysts for ammonia synthesis, *Nano Res.* Energy (2023) 1–10, <https://doi.org/10.26599/NRE.2023.9120068>.
- [24] R. Li, T. Gao, P. Wang, W. Qiu, K. Liu, Y. Liu, Z. Jin, P. Li, The origin of selective nitrate-to-ammonia electroreduction on metal-free nitrogen-doped carbon aerogel catalysts, *Appl. Catal. B Environ.* 331 (2023), 122677, <https://doi.org/10.1016/j.apcatb.2023.122677>.
- [25] M. Zhang, B. Yang, T. Yang, Y. Yang, Z. Xiang, A ferric citrate derived Fe-N-C electrocatalyst with stepwise pyrolysis for highly efficient oxygen reduction reaction, *Chin. Chem. Lett.* 33 (2022) 362–367, <https://doi.org/10.1016/j.ccl.2021.06.054>.
- [26] T. Gao, L. Qiu, M. Xie, Z. Jin, P. Li, G. Yu, Defect-stabilized and oxygen-coordinated iron single-atom sites facilitate hydrogen peroxide electrosynthesis, *D3MH00882G*, *Mater. Horiz.* 10 (2023) 1039, <https://doi.org/10.1039/D3MH00882G>.
- [27] J. Yang, H. Qi, A. Li, X. Liu, X. Yang, S. Zhang, Q. Zhao, Q. Jiang, Y. Su, L. Zhang, J.-F. Li, Z.-Q. Tian, W. Liu, A. Wang, T. Zhang, Potential-driven restructuring of Cu single atoms to nanoparticles for boosting the electrochemical reduction of nitrate to ammonia, *J. Am. Chem. Soc.* 144 (2022) 12062–12071, <https://doi.org/10.1021/jacs.2c02262>.
- [28] P. Li, L. Liao, Z. Fang, G. Su, Z. Jin, G. Yu, A multifunctional copper single-atom electrocatalyst aerogel for smart sensing and producing ammonia from nitrate, *Proc. Natl. Acad. Sci.* 120 (2023), e2305489120, <https://doi.org/10.1073/pnas.2305489120>.
- [29] X. Lu, H. Song, J. Cai, S. Lu, Recent development of electrochemical nitrate reduction to ammonia: a mini review, *Electrochem. Commun.* 129 (2021), 107094, <https://doi.org/10.1016/j.elecom.2021.107094>.
- [30] G.-F. Chen, Y. Yuan, H. Jiang, S.-Y. Ren, L.-X. Ding, L. Ma, T. Wu, J. Lu, H. Wang, Electrochemical reduction of nitrate to ammonia via direct eight-electron transfer using a copper-molecular solid catalyst, *Nat. Energy* 5 (2020) 605–613, <https://doi.org/10.1038/s41560-020-0654-1>.
- [31] T. Zhu, Q. Chen, P. Liao, W. Duan, S. Liang, Z. Yan, C. Feng, Single-atom Cu catalysts for enhanced electrocatalytic nitrate reduction with significant alleviation of nitrite production, *Small* 16 (2020) 2004526, <https://doi.org/10.1002/smll.202004526>.
- [32] H. Chen, C. Zhang, L. Sheng, M. Wang, W. Fu, S. Gao, Z. Zhang, S. Chen, R. Si, L. Wang, B. Yang, Copper single-atom catalyst as a high-performance electrocatalyst for nitrate-ammonium conversion, *J. Hazard. Mater.* 434 (2022), 128892, <https://doi.org/10.1016/j.jhazmat.2022.128892>.
- [33] X. Zhao, X. Jia, Y. He, H. Zhang, X. Zhou, H. Zhang, S. Zhang, Y. Dong, X. Hu, A. V. Kuklin, G.V. Baryshnikov, H. Ågren, G. Hu, Two-dimensional BCN matrix inlaid with single-atom-Cu driven electrochemical nitrate reduction reaction to achieve sustainable industrial-grade production of ammonia, *Appl. Mater. Today* 25 (2021), 101206, <https://doi.org/10.1016/j.apmt.2021.101206>.
- [34] W. Qiu, X. Chen, Y. Liu, D. Xiao, P. Wang, R. Li, K. Liu, Z. Jin, P. Li, Confining intermediates within a catalytic nanoreactor facilitates nitrate-to-ammonia electrosynthesis, *Appl. Catal. B Environ.* 315 (2022), 121548, <https://doi.org/10.1016/j.apcatb.2022.121548>.
- [35] T. Yang, X. Mao, Y. Zhang, X. Wu, L. Wang, M. Chu, C.-W. Pao, S. Yang, Y. Xu, X. Huang, Coordination tailoring of Cu single sites on C3N4 realizes selective CO₂ hydrogenation at low temperature, *Nat. Commun.* 12 (2021) 6022, <https://doi.org/10.1038/s41467-021-26316-6>.
- [36] Y. Zhou, F. Wei, H. Qi, Y. Chai, L. Cao, J. Lin, Q. Wan, X. Liu, Y. Xing, S. Lin, A. Wang, X. Wang, T. Zhang, Peripheral-nitrogen effects on the Ru1 centre for highly efficient propane dehydrogenation, *Nat. Catal.* (2022), <https://doi.org/10.1038/s41929-022-00885-1>.
- [37] Y. Pan, Y. Chen, K. Wu, Z. Chen, S. Liu, X. Cao, W.-C. Cheong, T. Meng, J. Luo, L. Zheng, C. Liu, D. Wang, Q. Peng, J. Li, C. Chen, Regulating the coordination structure of single-atom Fe-NxCy catalytic sites for benzene oxidation, *Nat. Commun.* 10 (2019) 4290, <https://doi.org/10.1038/s41467-019-12362-8>.
- [38] C. Du, Y. Gao, H. Chen, P. Li, S. Zhu, J. Wang, Q. He, W. Chen, A Cu and Fe dual-atom nanzyme mimicking cytochrome c oxidase to boost the oxygen reduction reaction, *J. Mater. Chem. A* 8 (2020) 16994–17001, <https://doi.org/10.1039/D0TA06485H>.
- [39] Z. Jin, P. Li, Y. Meng, Z. Fang, D. Xiao, G. Yu, Understanding the inter-site distance effect in single-atom catalysts for oxygen electroreduction, *Nat. Catal.* 4 (2021) 615–622, <https://doi.org/10.1038/s41929-021-00650-w>.
- [40] N. Zhang, T. Zhou, M. Chen, H. Feng, R. Yuan, C. Zhong, W. Yan, Y. Tian, X. Wu, W. Chu, C. Wu, Y. Xie, High-purity pyrrole-type FeN₄ sites as a superior oxygen reduction electrocatalyst, *Energy Environ. Sci.* 13 (2020) 111–118, <https://doi.org/10.1039/C9EE03027A>.
- [41] K. Zhao, X. Nie, H. Wang, S. Chen, X. Quan, H. Yu, W. Choi, G. Zhang, B. Kim, J. G. Chen, Selective electroreduction of CO₂ to acetone by single copper atoms anchored on N-doped porous carbon, *Nat. Commun.* 11 (2020) 2455, <https://doi.org/10.1038/s41467-020-16381-8>.
- [42] N. Zhang, T. Zhou, M. Chen, H. Feng, R. Yuan, C. Zhong, W. Yan, Y. Tian, X. Wu, W. Chu, C. Wu, Y. Xie, High-purity pyrrole-type FeN₄ sites as a superior oxygen reduction electrocatalyst, *Energy Environ. Sci.* 13 (2020) 111–118, <https://doi.org/10.1039/C9EE03027A>.
- [43] J. Zhang, Z. Zhao, Z. Xia, L. Dai, A metal-free bifunctional electrocatalyst for oxygen reduction and oxygen evolution reactions, *Nat. Nanotechnol.* 10 (2015) 444–452, <https://doi.org/10.1038/nnano.2015.48>.
- [44] R. Li, T. Gao, W. Qiu, M. Xie, Z. Jin, P. Li, Unveiling the size effect of nitrogen-doped carbon-supported copper-based catalysts on nitrate-to-ammonia electroreduction, *Nano Res.* (2023), <https://doi.org/10.1007/s12274-023-6094-z>.
- [45] J. Zhang, C. Zheng, M. Zhang, Y. Qiu, Q. Xu, W.-C. Cheong, W. Chen, L. Zheng, L. Gu, Z. Hu, D. Wang, Y. Li, Controlling N-doping type in carbon to boost single-atom site Cu catalyzed transfer hydrogenation of quinoline, *Nano Res.* 13 (2020) 3082–3087, <https://doi.org/10.1007/s12274-020-2977-4>.
- [46] P. Li, Z. Jin, Y. Qian, Z. Fang, D. Xiao, G. Yu, Supramolecular confinement of single Cu atoms in hydrogel frameworks for oxygen reduction electrocatalysis with high atom utilization, *Mater. Today* 35 (2020) 78–86, <https://doi.org/10.1016/j.mattod.2019.10.006>.
- [47] Y.-T. Xu, M.-Y. Xie, H. Zhong, Y. Cao, In situ clustering of single-atom copper precatalysts in a metal-organic framework for efficient electrocatalytic nitrate-to-ammonia reduction, *ACS Catal.* 12 (2022) 8698–8706, <https://doi.org/10.1021/acscatal.2c02033>.
- [48] K. Wu, C. Sun, Z. Wang, Q. Song, X. Bai, X. Yu, Q. Li, Z. Wang, H. Zhang, J. Zhang, X. Tong, Y. Liang, A. Khosla, Z. Zhao, Surface reconstruction on uniform Cu nanodisks boosted electrochemical nitrate reduction to ammonia, *ACS Mater. Lett.* 4 (2022) 650–656, <https://doi.org/10.1021/acsmaterialslett.2c00149>.
- [49] Y. Wang, A. Xu, Z. Wang, L. Huang, J. Li, F. Li, J. Wicks, M. Luo, D.-H. Nam, C.-S. Tan, Y. Ding, J. Wu, Y. Lum, C.-T. Dinh, D. Sinton, G. Zheng, E.H. Sargent, Enhanced nitrate-to-ammonia activity on copper-nickel alloys via tuning of intermediate adsorption, *J. Am. Chem. Soc.* 142 (2020) 5702–5708, <https://doi.org/10.1021/jacs.9b13347>.